JMEPEG (2021) 30:1387–1397
https://doi.org/10.1007/s11665-020-05356-x

1059-9495/$19.00

Effect of Y_2O_3 on Mechanical and Corrosion Properties of Fe and Fe-Ni Alloys Prepared by Mechanical Alloying Followed by Spark Plasma Sintering

Arpan Arora, Atul Kumar, and Suhrit Mula

Submitted: 12 May 2020 / Revised: 5 November 2020 / Accepted: 14 November 2020 / Published online: 5 January 2021

In the present study, Fe-42% Ni, Fe-2% Y_2O_3, and Fe-42% Ni-2% Y_2O_3 (30-60 nm) were prepared by mechanical alloying using high energy SPEX8000M ball mill. Consolidation of the milled sample was done by spark plasma sintering (SPS) at 800, 900, and 1000 °C at a pressure of 60 MPa with a holding period of 5 min in an argon atmosphere. The sintered density was found to be higher at a higher temperature, e.g., 98% at 1000 °C as compared to 78% at 800 °C. The addition of nanosize Y_2O_3 in Fe or Fe-Ni system showed a strong influence on the formation of intermetallic compounds and final grain size of the resultant material. x-ray diffraction analysis of the sintered Fe-42% Ni-2% Y_2O_3 alloy indicates the presence of Fe-Ni phase with additional peaks of intermetallic phases ($Fe_{17}Y_2$, Ni_5Y) and oxides (Fe_3O_4, NiO). The nanoindentation hardness of the sintered (at 1000 °C) alloys was found to be the maximum for the Fe-42% Ni-2% Y_2O_3 (7.9 GPa), followed by Fe-2% Y_2O_3 (7.2 GPa) and Fe-42% Ni alloy (5.8 GPa). Dry sliding wear resistance of the spark plasma sintered (SPSed) (sintered at 1000 °C) Fe-42% Ni-2% Y_2O_3 was found to improve due to higher hardness and formation of oxide rich layer at the contact surface. Moreover, the SPSed specimen of the Fe-42% Ni-2% Y_2O_3 alloy showed a better corrosion resistance (I_{corr} = 0.78 µA/cm^2) as compared to the corrosion resistance (I_{corr} = 1.34 µA/cm^2) of the Fe-42% Ni alloy, both sintered at 1000 °C. The corrosion tests were conducted in a freely aerated 3.5% solution of NaCl electrolyte. A significant amount of grain refinement (due to the addition of nanosize yttria), formation of intermetallic phases ($Fe_{17}Y_2$, Ni_5Y) as well as uniform distribution of fine oxide particles (Fe_3O_4, NiO) played the pivotal role in the improvement of wear, corrosion and mechanical properties of the SPSed Fe-42% Ni-2% Y_2O_3 alloy.

Keywords ball milling, corrosion resistance, electron microscopy, grain refinement, intermetallic phase, spark plasma sintering

1. Introduction

Owing to the unique combination of properties like high strength, superior magnetic properties, iron-based alloys are preferred for a wide variety of applications, including structural, magnetic, and automobile applications (Ref 1-3). The mechanical and corrosion properties can be further improved by alloying with suitable elements (Ref 3). Due to the versatile beneficial nature of Ni, it is highly popular in the research of iron-based alloys among all known alloying elements. The addition of Ni in Fe shows not only good mechanical properties but also improves chemical inertness and toughness of iron-based materials (Ref 1-3). Thus, Fe-Ni alloys have excellent mechanical, wear, thermal, and magnetic properties and could be produced in large quantities easily (Ref 1, 2). They are also being used in a variety of forms including thin coatings, self-supporting sheets, tubes and foils, and complex geometries. Fe-based alloys containing Ni also shows good corrosion resistance. For example, Singh et al. (Ref 3) added 10-50 wt.% Ni in Fe system. They reported that the Fe with 50 wt.% Ni has better corrosion resistance than that of the other low Ni content alloys. This is explained to the formation of the maximum amount of γ phase, which helped in improving the corrosion resistance (Ref 3). Alharthi et al. (Ref 4) investigated the effect of Ni content on the corrosion resistance behavior of Fe-36% Ni alloy and Fe-45% Ni alloys in 1 M concentration HCl solution. They reported that Fe with 45 wt.% of Ni showed better corrosion resistance than that of Fe-36% Ni alloy. The formation of thicker impervious oxides film in case of higher Ni content alloy (Fe-45% Ni) protects it from being easily corroded (Ref 4). Invar (Fe-36% Ni) and super-invar (Fe-42% Ni) are well-known materials for parts having a low coefficient of thermal expansion and good mechanical strength (Ref 5), whereas Fe with 50% Ni has superior magnetic behavior (Ref 1, 6). Ni is γ-stabilizer in iron, which retard the fcc to bcc transition temperature and helps in developing commercial austenitic steel. On the other hand, increasing the fraction of Ni in Fe-Ni alloy causes a decrease in the corrosion rate and increases the wear rate (i.e., decrease in wear resistance) (Ref 3, 7, 8).

Therefore, the development of Fe-Ni based oxide nanocomposites has been a potential research field due to its excellent corrosion and wear resistance, high strength and fracture toughness, and good magnetic properties (Ref 8). It could also be great materials for a large number of applications such as catalysts, recording heads, shielding of magnetic materials,

Arpan Arora and **Suhrit Mula**, Metallurgical and Materials Engineering Department, IIT Roorkee, Roorkee, India; and **Atul Kumar**, School of Mechanical Engineering, Vellore Institute of Technology, Vellore, India. Contact e-mails: suhrit.mula@mt.iitr.ac.in and suhritmula@gmail.com.

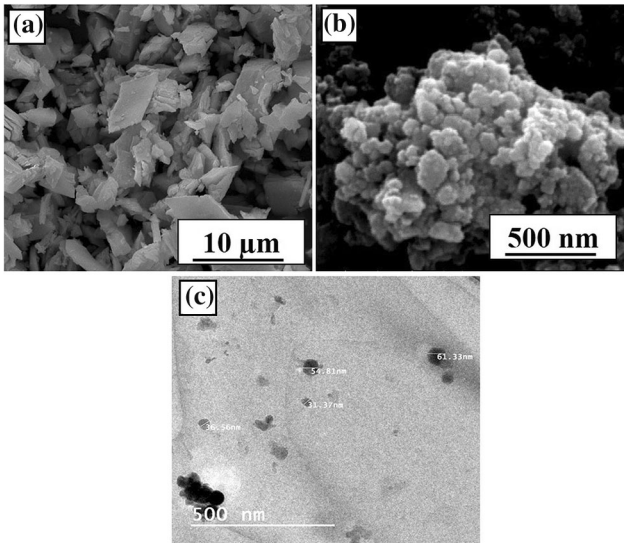

Fig. 1 SEM images of Y_2O_3 powder particles in (a) as received and (b) 40 h milled condition; (c) TEM image of 40 h milled Y_2O_3 powder particles

high-performance transformers. The addition of ultrafine oxide particles in Fe-based alloys (usually Y_2O_3), restrict the grain boundary sliding and retards grain coarsening, thereby significantly improves the creep strength (Ref 8). It is also reported that the addition of Y_2O_3 can increase the toughness of structurally amorphous metals by interrupting the shear band formation (Ref 9). Kotan et al. (Ref 10) reported that the addition of 1 and 3 wt.% Y_2O_3 particles in $Fe_{91}Ni_8Zr_1$ could cause an increase in hardness to 7.5 and 8 GPa, respectively. Y_2O_3 acts as a grain size stabilizer that can restrict the grain growth and BCC to FCC transformation at high temperature ($T > 700$ °C). Sun et al. (Ref 11) reported that addition of Y_2O_3 (0.6 wt.%) in Ni-20% Cr-5% Al alloy increased its oxidation resistance. It is due to the formation of stable oxide layer and better adhesion between oxide scale and matrix.

It is now well-known that mechanical alloying has the ability to synthesize a variety of metastable phases ranging from elemental powder mixtures to pre-gelatinized powders with brittle–brittle or ductile–ductile combination of materials (Ref 12). The consolidation of powder mixtures by SPS allows achieving high density with considerable restriction in the grain coarsening (Ref 13-15). However, the preparation of iron-nickel-yttria alloys by MA + SPS and characterization of sintered alloys are not explored considerably. In this context, Fe-42 wt.% Ni, Fe-2 wt.% Y_2O_3, and Fe-42 wt.% Ni-2 wt.% Y_2O_3 compositions* were prepared by high energy ball milling and consolidated by SPS at 800, 900, and 1000 °C. Their microstructural evolution and mechanical properties have been investigated and correlated with their corresponding microstructure and different strengthening mechanisms involved. Also, the role of Ni and nanosize Y_2O_3 has been analyzed in detail.

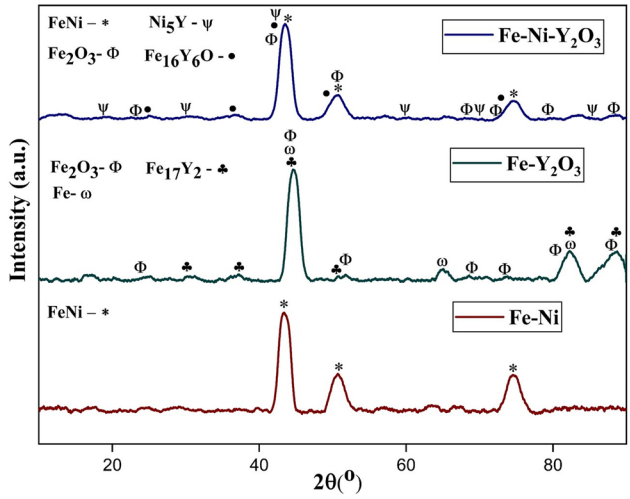

Fig. 2 XRD pattern of Fe-42% Ni, Fe-2% Y_2O_3 and Fe-42% Ni-2% Y_2O_3 milled samples

2. Experimental

2.1 Alloy Preparation

Y_2O_3 powder (99.9% purity, average particle size of 44 μm, Alfa Aesar) was ball-milled to reduce its size to nanometer level by a planetary ball mill (Retsch, PM400, Germany) using a tungsten carbide vial and tungsten carbide balls. The mechanical milling was done for 40 h at 270 rpm, maintaining a ball to powder ratio of 10:1. Milling was conducted under toluene to control the generation of heat and avoid agglomeration of fine particles produced. SEM study confirmed that the final particle size was in the range of 30-60 nm. The milled Y_2O_3 (30-60 nm) particles were added to blend compositions of Fe and Fe-42% Ni prior to mechanical alloying (MA) in a high energy ball mill (Spex 8000 M, USA). Fe and Ni powders of 10 μm and 44 μm, respectively, were also procured from Alfa Aesar with 99.5% purity. The MA of the final compositions Fe-42% Ni, Fe-2% Y_2O_3 and Fe-42% Ni-2% Y_2O_3 was performed for 25 h in chrome-steel vial loaded with stainless steel balls with a ball to powder weight ratio of 10:1. The milled composition was poured in a graphite die-punch arrangement (10 mm diameter) and consolidated by spark plasma sintering (SPS 625, Dr. Sinter, Fuji Electronics Ltd., Japan) in an argon atmosphere at a 60 MPa pressure for 5 min at 800, 900, and 1000 °C. The rate of heating was maintained at 100 °C/min for all the samples. The density of sintered specimens was measured by the Archimedes method using a density measurement kit (ML204/A01, METTLER TOLEDO, Switzerland).

2.2 X-ray Diffraction

The powders and sintered samples were subjected to x-ray diffraction study by Rigaku x-ray diffractometer using a CuKα ($\lambda = 0.154$ nm) radiation at a scan rate of 1°/min. For identifying different phases and removing the background noise, X'pert high score plus software was used.

*All compositions are in wt.%; hence onwards, it will be written as Fe-42% Ni, Fe-2% Y_2O_3, and Fe-42% Ni-2% Y_2O_3, respectively.

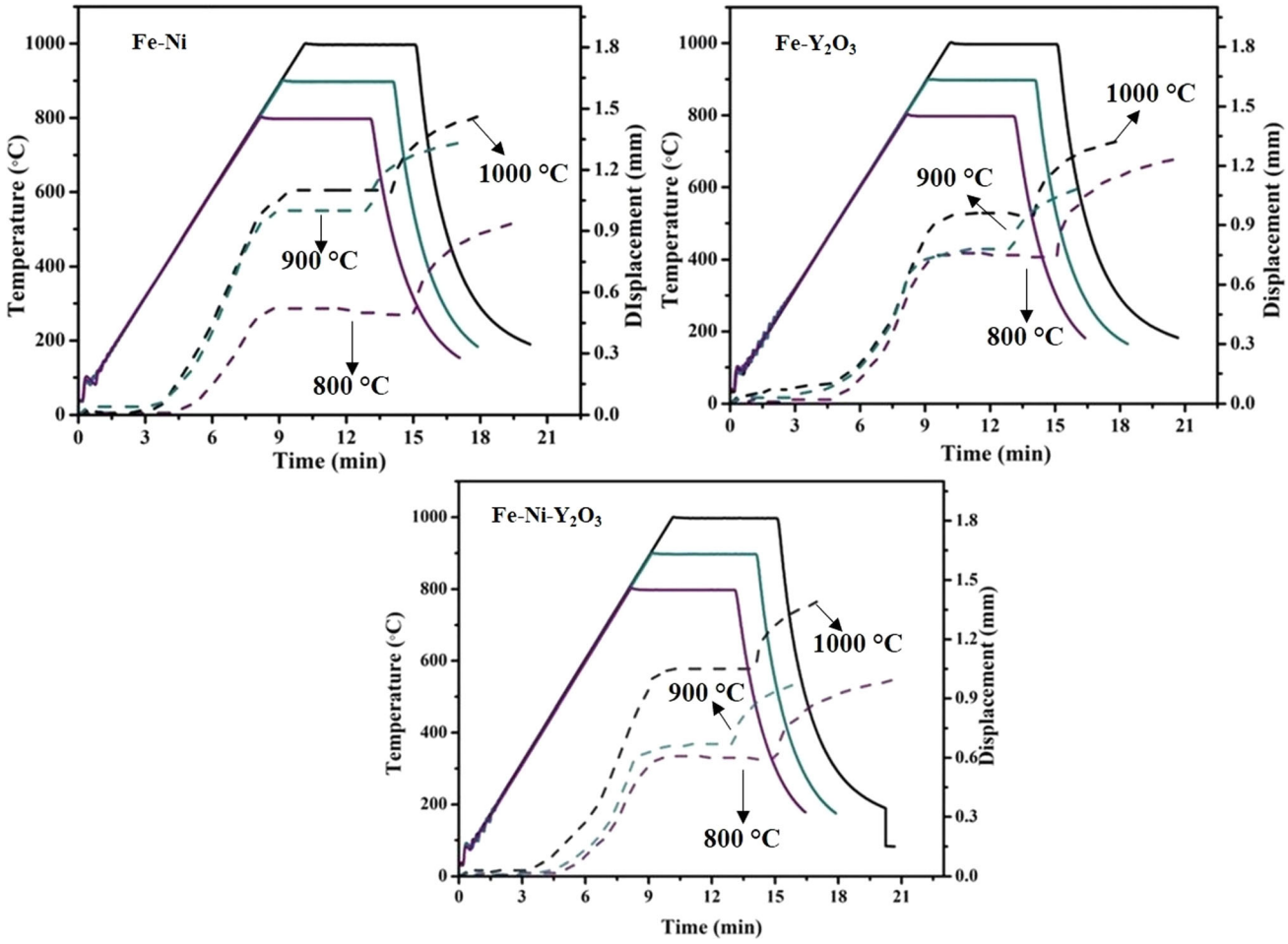

Fig. 3 Spark plasma sintering profiles between time, temperature, and displacement during consolidation of the samples

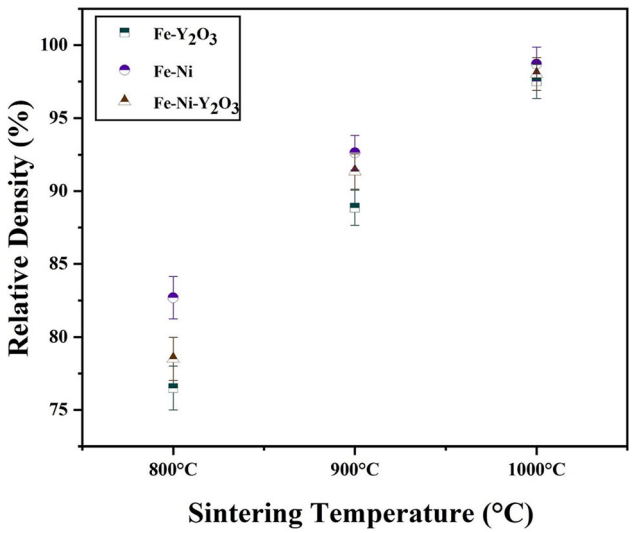

Fig. 4 Relative sintered density of different SPSed compositions sintered at different temperatures

2.3 Microstructural Study by Optical Microscopy and SEM

The samples of the sintered alloys were prepared using standard techniques involving different grades of emery papers + cloth polishing. Polished surfaces were subjected to etching using Nital (5% HNO_3 + 95% ethanol) for 5-15 s. Microstructures of the etched surfaces were captured using an optical microscope (Leica, 500 M, Germany).

A scanning electron microscope (FEI-Quanta 200, FE-SEM, Netherland) equipped with an energy dispersive x-ray spectroscopy (EDS) set-up was used to study microstructural features of the milled powder, sintered samples, and worn out surfaces after wear testing.

2.4 Hardness Measurement

Microhardness measurement of the sintered specimens was performed using a Vickers hardness tester (Buehler Micrometer II) with a 50 g load for a residence time of 5 s. Nanoindentation testing was conducted using a Triboindenter (Hysitron TI950 Hysitron Inc, USA) having three-sided Berkovich diamond indenter of 100 nm tip diameter. A normal load of 5000 μN/s was applied at a constant loading and unloading rate of 400 μN/s with a dwell time of 2 s for nanoindentation testing.

2.5 Wear Resistance Analysis

Wear behavior of the sintered specimens was studied using a ball-on-disk tribometer (TR-201E-M2, DUCOM, Bangalore, India) in dry conditions with commercially available 10-mm-diameter alumina ball (Vickers hardness of 16 GPa, RGP, Bangalore, India). The alumina ball was kept stationary, and the sintered sample was rotated at 500 rpm at an initial track

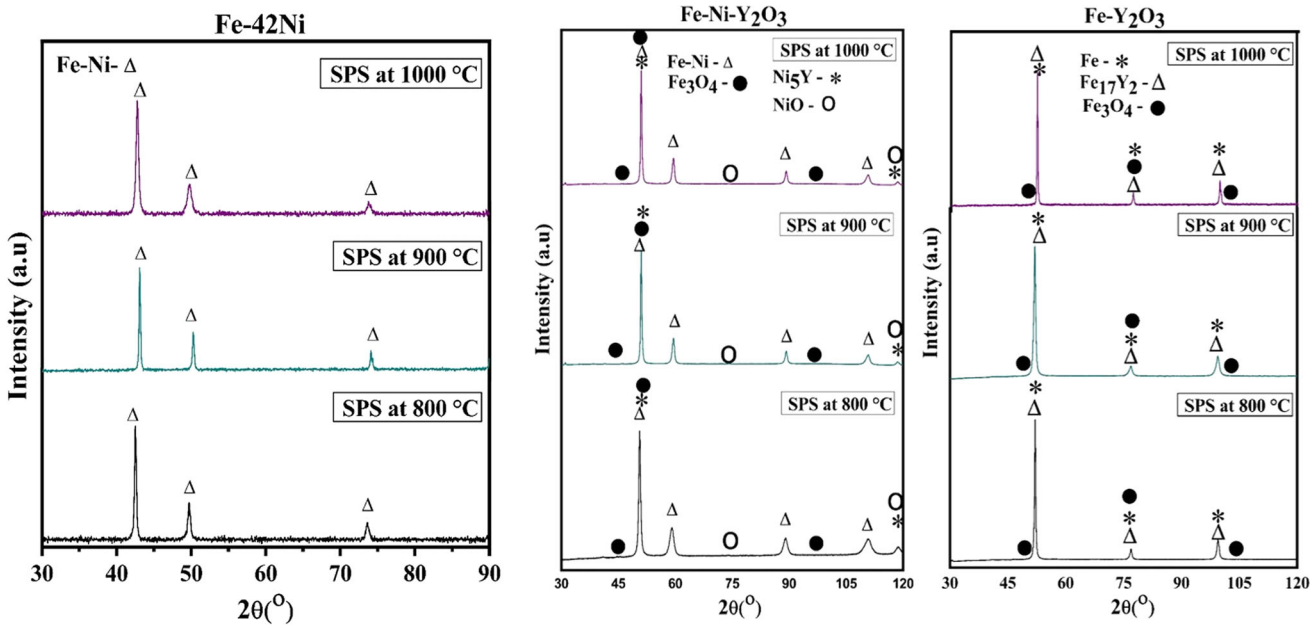

Fig. 5 XRD pattern of Fe-42% Ni, Fe-2 Y_2O_3, and Fe-42% Ni-2% Y_2O_3 sintered samples

radius of 5 mm. The wear test was conducted for 30 min under different applied loads of 5, 10, and 20 N at ambient conditions, i.e., at room temperature and 45-50% RH. The coefficient of friction generated during the wear test was recorded online with the attached computer interface. A stylus-tip profilometer (SJ 400, Mitutoyo, Japan) was used to measure the depth of wear track in transverse to the sliding direction. At least six measurements were taken to represent the average depth for each worn surface. In addition, worn out surfaces of the investigated alloys were examined using SEM equipped with EDS identify the dominant wear mechanisms.

2.6 Corrosion Testing

Corrosion behavior of the sintered samples was studied in a round bottom cell with a saturated calomel electrode as the reference electrode. Tests were conducted using Gamry potentiostat (model: Interface1000) in a freely aerated 3.5% solution of NaCl electrolyte. Tafel extrapolation analysis was used to determine the corrosion rate. Each test was performed twice to check the reproducibility of the electrochemical polarization behavior.

3. Results and Discussion

3.1 Characterization of Yttria Powder and Ball-Milled Blend Compositions

As received, Y_2O_3 powder (average size 44 μm) was mechanically milled for 40 h in a planetary ball mill to obtain nanometer-size particles of the same. Figure 1(a) and (b) shows SEM images of Y_2O_3 particles before and after the milling (i.e., as received and 40 h milled samples).

The average size of the yttria powder particles decreased to ~ 1 μm after 20 h of milling, while it was reduced to 30-60 nm after milling for 40 h. Further, the agglomeration of fine powder particles is evident in the Fig. 1(b). In order to ascertain the size of the 40 h milled Y_2O_3 particles, the agglomeration was eliminated by ultrasonication in acetone, and TEM images were taken for powder particles (Fig. 1c). The TEM image in Fig. (1c), clearly shows that the particle sizes are in the nanometer range. The de-agglomerated particles were dried up before adding to the blend compositions. The high energy ball mill was used for mechanical alloying of the blend compositions of Fe, Ni, and nanosize Y_2O_3 powders.

XRD patterns of the milled samples are shown in Fig. (2). It shows the formation of Fe-Ni phase when 42% Ni is added in iron powder and mechanically alloyed for 25 h. Further, $Fe_{17}Y_2$, Fe_2O_3 phases are found to form after the addition of Y_2O_3 nanosize powder in iron and subsequent milling for 25 h. On the other hand, the XRD analysis of Fe-42% Ni-2% Y_2O_3 milled sample reveals the formation of Ni_5Y intermetallic phase in addition to Fe_2O_3 and $Fe_{16}Y_6O$. During mechanical milling of the ODS steels containing Y_2O_3, processes of intra particle cold-welding and shearing occur continuously due to severe plastic deformation between the powder particles (Ref 16-18). Thus, exchange of matters takes place between powder grains, simultaneously by mechanical mixing (through welding and fracturing) and diffusion of atoms within the grains of different particles. After desired duration of milling, all grains of powder particles achieve equivalent average chemical composition. At that point, matrix grains are not completely homogeneous at the atomic scale. Then further milling of the resultant structure continues to create numerous vacancies within the grains due to continuous welding and shearing. Thus, these vacancies allow a very fast diffusion to take place at the atomic level evolving a complete solid solution supersaturated with Y and O. If enough activation energy is available, as happened in the present study, favorable oxides and/or intermetallic phase could be evolved during mechanical alloying itself. Thus, the addition of a small amount of Y_2O_3 powder in Fe or Fe-Ni leads to the formation of intermetallic compounds along with the evolution of some complex nanoclusters/oxide phases.

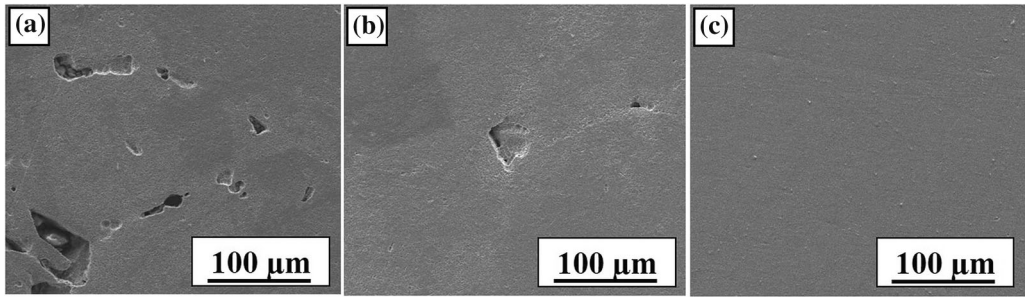

Fig. 6 SEM images of Fe-42% Ni alloy sintered at (a) 800 °C, (b) 900 °C, and (c) 1000 °C

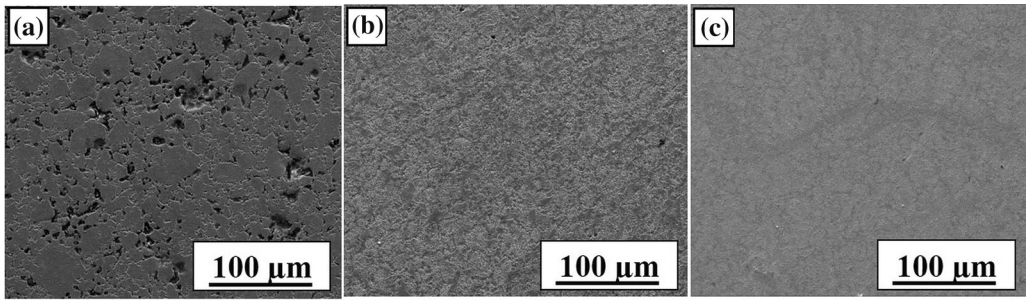

Fig. 7 SEM images of Fe-2% Y_2O_3 alloy sintered at (a) 800 °C, (b) 900 °C, and (c) 1000 °C

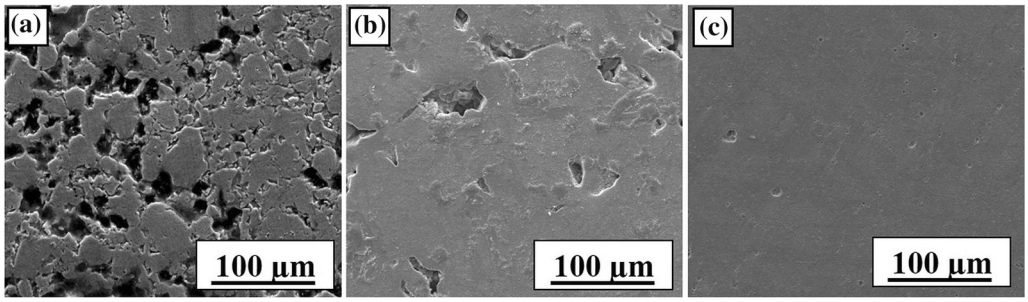

Fig. 8 SEM images of Fe-42% Ni-2% Y_2O_3 alloy sintered at (a) 800 °C, (b) 900 °C, and (c) 1000 °C

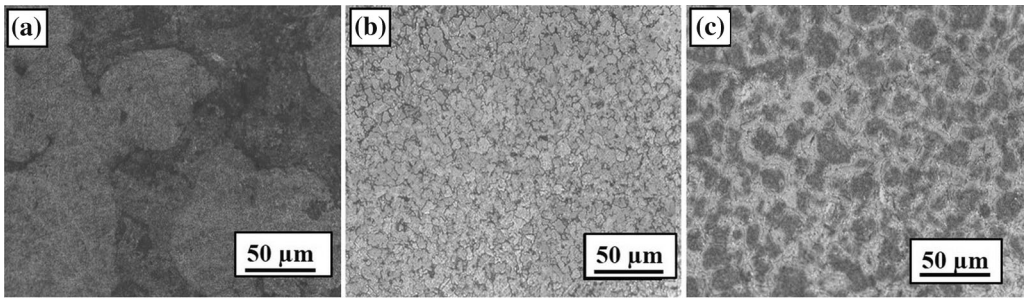

Fig. 9 Optical microscopy images of (a) Fe-42% Ni, (b) Fe-2% Y_2O_3, and (c) Fe-42% Ni-2% Y_2O_3 alloy sintered at 1000 °C

3.2 Spark Plasma Sintering

Typical spark plasma sintering (SPS) profiles (i.e., Time–Temperature–Displacement plots) for the investigated compositions are shown in Fig. 3. For given alloys, larger displacement is found when sintering was done at a higher temperature (1000 °C), indicating better densification. The (wave logger) inbuilt software with the SPS machine was used to understand the temperature graph and displacement during the real-time of sintering. It was found that the displacement increases with an increase in the sintering temperature for all the compositions. Time, pressure, and temperature are the three major factors for the displacement in the sintered sample. In the initial stage, wave curve of displacement was proportional to the temperature. With increasing temperature, the mechanism of diffusion

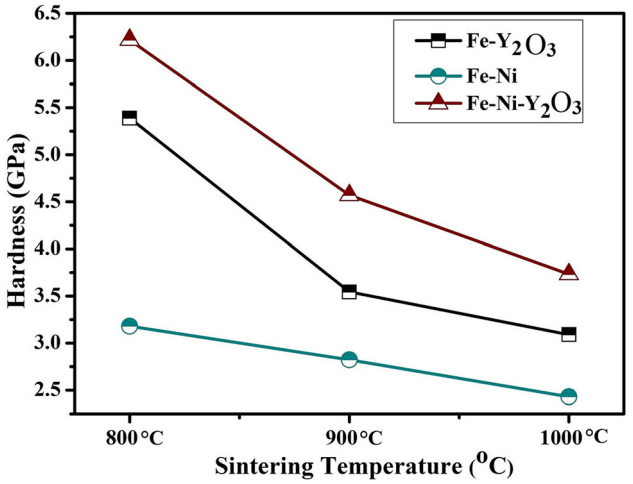

Fig. 10 Variation in microhardness of the different SPSed samples as a function of sintering temperature

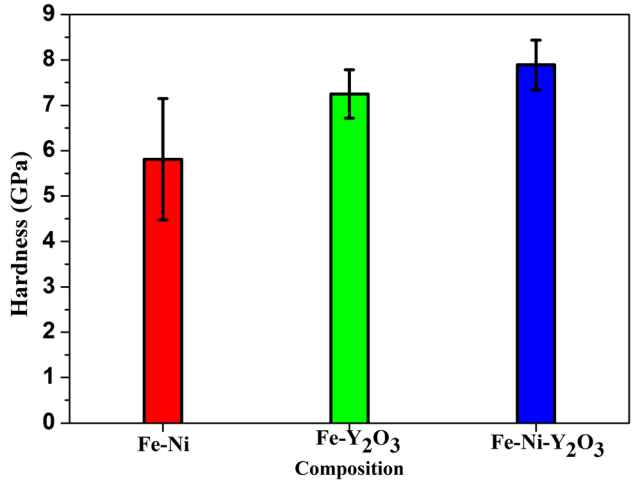

Fig. 11 Variation of nanoindentation hardness as a function of compositions (Fe-42% Ni, Fe-2% Y_2O_3, and Fe-42% Ni-2% Y_2O_3) sintered at 1000 °C

and mass transportation increases at a large scale between the adjacent neighboring particles. In the second stage, curve shows the holding period, where the temperature is constant (isothermal) at 800/900/1000 °C. In the last stage, i.e., during cooling, it was found that the displacement increases irrespective of temperature, mainly due to the shrinkage of the sample (Ref 20).

Theoretical density of the alloys was calculated using rule of mixtures, $\rho = w_1\rho_1 + w_2\rho_2 + w_3\rho_3$; where, w_1, w_2, and w_3 are the weight fraction, and ρ_1, ρ_2, and ρ_3 are the density of components of the three different materials, respectively. The theoretical density of the compositions was found to be 8.307 g/cm^3, 7.81 g/cm^3 and 8.25 gm/cm^3 for Fe-42% Ni, Fe-2% Y_2O_3, and Fe-42% Ni-2% Y_2O_3, respectively. The relative sintered density of the investigated alloys is shown in Fig. 4, corresponding to three different sintering temperatures. The density of alloys sintered at 800 °C was found to be the least (only $\sim$ 76%) for Fe-42% Ni-2% Y_2O_3 alloy. With the increase in temperature to 1000 °C, the maximum density of 98.5% is achieved in case of the Fe-42% Ni alloy. Overall, the average density increased with increase in the sintering temperature. It is mainly due to the decrease in the total porosity of the sample with the increase in the sintering temperature (Ref 21, 22) (detail is discussed later in Sect. 3.4).

3.3 Phase Analysis of the Sintered Samples

XRD phase analysis of Fe-42% Ni, Fe-2% Y_2O_3, and Fe-42% Ni-2% Y_2O_3 alloys sintered at three different temperatures (800, 900, and 1000 °C) shows the evolution of various phases (Fig. 5). In Fe-42% Ni alloy, the peak identified to be only Fe-Ni alloy. There was no other intermetallic phase or oxide peaks found, as the solubility of Ni in Fe is very high, which forms substitutional solid solution of Ni in Fe, consequently forms Fe-Ni austenitic phase (Ref 23). Phase evolution characteristic is not changed with change in sintering temperature. On the other hand, Fe-matrix is identified to be the major phase along with the evolution of $Fe_{17}Y_2$ and Fe_3O_4 in Fe-2% Y_2O_3 alloy.

The formation of $Fe_{17}Y_2$ phase occurs in Fe-2% Y_2O_3 containing Y_2O_3 is that the added oxide first gets dissolved into the metallic matrix after suitable time of milling (25 h) (described in detail earlier Sect. 3.1) and thereafter, nanosize clusters formation could be achieved either during mechanical alloying itself, if required activation energy is available or by sintering at suitable temperature and/or thermomechanical treatment (Ref 16). However, the endorsement of this mechanism is solely established on the basis of various characterization of such final material's composition. Evolution of a thinner nano-oxides dispersion is also reported during mechanical milling having a very pure milling atmosphere (Ref 16, 24, 25). Through ab initio calculations in iron, Fu et al. (Ref 19) reported that, when pre-existed vacancies are available within the material (e.g., in a milled sample), the formation energy of O-vacancy pair essentially disappears. Therefore, these an O-vacancy pairs attract those atoms which have more affinity to oxygen. Thus, this O-vacancy mechanism possibly promotes the formation of O-, Y- and Fe-enriched complex nanoclusters (Ref 16, 19). Ni_5Y is observed to form in Fe-42% Ni-2% Y_2O_3 in addition to Fe_3O_4 and NiO phases. Fe_2O_3 present in the 25 h milled samples (as shown in Fig. 2) was transformed to Fe_3O_4 due to reduction while sintering occur at 800 to 1000° C temperature (Ref 26). Thus, the formation of new oxides and intermetallic phases is observed to form in the spark plasma sintered (SPSed) alloys as compared to the milled powder samples.

3.4 Microstructural Characterization

The micrographs of the spark plasma sintered (SPSed) samples are shown in Fig. 6, 7 and 8. At low sintering temperature of 800 °C, the microstructure of Fe-42% Ni alloy shows less porosity as compared to all other investigated alloys (Fe-2% Y_2O_3 and Fe-42% Ni-2% Y_2O_3). However, all three alloy samples showed a very less amount of porosity when sintered at high temperature (1000 °C). The samples corresponding to Fig. 6, 7, and 8 were not etched in order to show the porosity variations clearly. Typical SEM images (as shown Fig. 6 and 7) of the SPSed samples clearly depicted that there is a considerable decrease in porosity (along with an increase in density) with an increase in the sintering temperature from 800 to 1000 °C.

Optical microscopy images of all the alloy samples (Fe-42% Ni, Fe-2% Y_2O_3, and Fe-42% Ni-2% Y_2O_3) sintered at 1000 °C

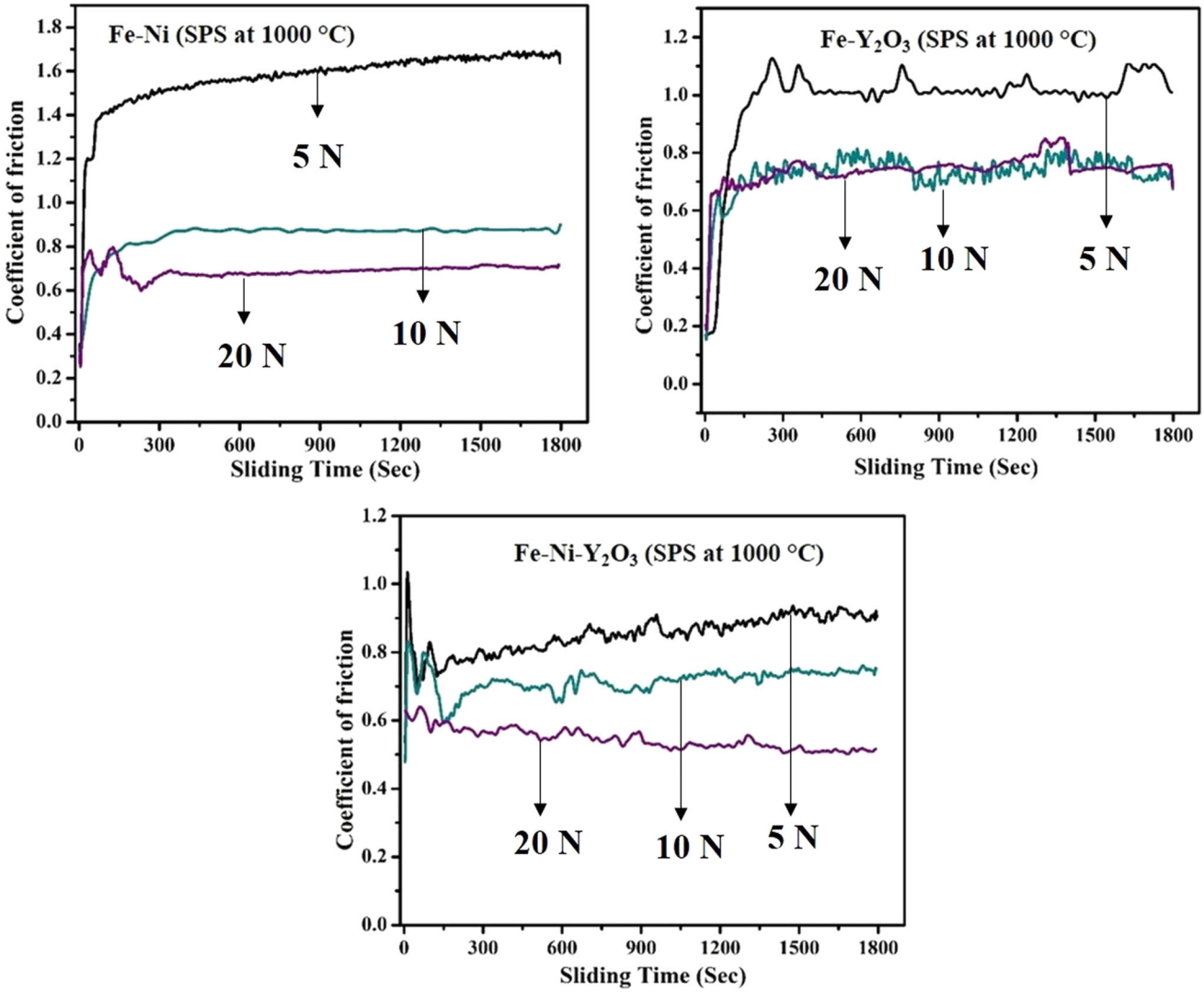

Fig. 12 Variation of COF with change in load (5 N to 20 N) for alloys sintered at 1000 °C

are shown in Fig. 9. It could be observed from Fig. 9 that the grains become more or less spherical in shape with a smooth surface. The dominant mechanism behind the densification is the atomic diffusion by mass transportation, which starts even at a low sintering temperature (with the formation of necks between particles) and continues to consolidate fully due to surface as well as grain boundary diffusion at high temperature (Ref 27). It is also observed from Fig. 9, that the alloy compositions containing Y_2O_3, i.e., Fe-2% Y_2O_3 and Fe-42% Ni-2% Y_2O_3 showed very good refinement in the final grain size. The mechanism behind the refinement is the retardation of grain growth by complex oxides, and intermetallic phases evolved due to the addition of nanosize Y_2O_3 particles. The locking of grain boundaries by these second phase particles in Fe and Fe-42% Ni matrix retards the grain growth, which ultimately leads to the development of fine grain structure.

3.5 Hardness of SPSed Samples

Microhardness values measured by Vicker's indentation test are shown in Fig. 10. The Vicker's hardness of the SPSed samples is found to vary from 2.5 to 6.2 GPa. It is to be noted that indentation was made within the bigger size particles to avoid any porosity effect. It is observed that the hardness of sintered samples at low sintering temperature (at 800 °C) is high (6.2 GPa) as the grains are smaller in size. With increasing sintering temperature, the grain size and sintered density both increased. Although the higher sintered density is achieved at high sintering temperature, the hardness value is found to decrease. It could be ascribed to the fact that increase in the hardness value due to higher sintered density could not overcompensate the decrease in the hardness resulted from grain coarsening. Among the investigated alloys, the hardness of Fe-42% Ni-2% Y_2O_3 is found to be higher as Y_2O_3 played an important role in the resultant grain refinement. In contrast, the hardness of Fe-42% Ni is found to be least (2.4 GPa) due to the maximum level of grain growth. Though Ni played an important role in grain refinement, it is restricted to a limited extent (i.e., 6-10%). The increase in the hardness due to decrease in grain size can also be explained through the Hall–Petch relation (Ref 28).

The dense samples (sintered at 1000 °C) were further investigated by nanoindentation testing. The hardness values of different alloys are shown in Fig. 11. It is to be noted that the

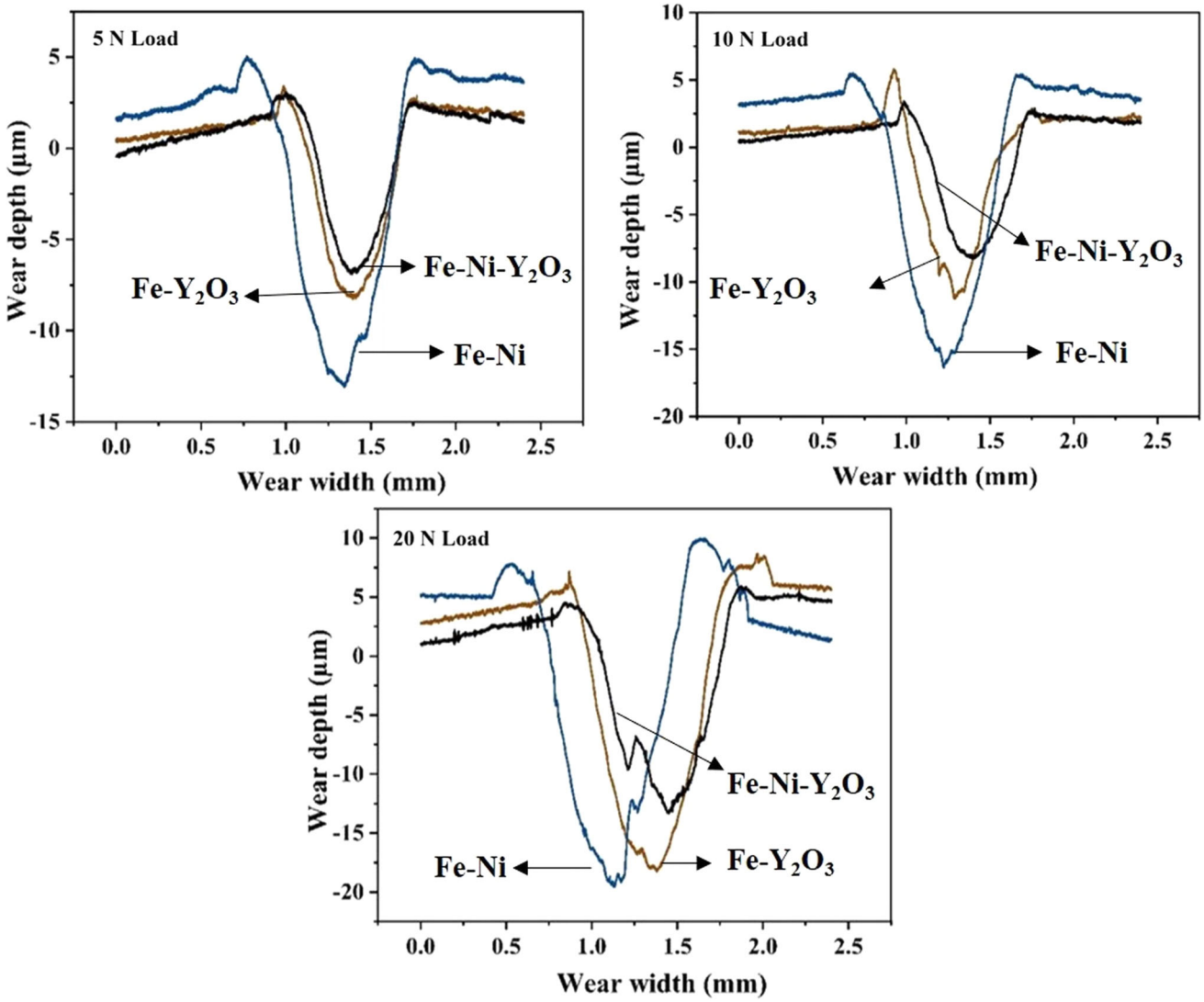

Fig. 13 Surface profiles of wear track of the alloys sintered at 1000 °C

absolute values of hardness obtained from Vickers and nanoindentation tests are found to be quite different. Nanoindentation hardness value for a specific sample is found to be more as compared to the Vickers hardness value. However, the trend of hardness variation with respect to compositions of the SPSed samples (sintered at 1000 °C) is found to be the same. The direct comparison in both the techniques is not justified owing to the difference in tip geometry, measurement length scale, and the vast difference in the applied loads (Ref 29).

3.6 Wear Behavior

Ball-on-disc wear tests were performed against 10-mm-diameter alumina ball at different loads, i.e., 5, 10, and 20 N. The wear tests were conducted on the polished surface of the SPSed Fe-42% Ni, Fe-2% Y_2O_3, and Fe-42% Ni-2% Y_2O_3 samples sintered at 1000 °C. The average coefficient of friction (COF) is found to vary in a range from 0.5 to 1.7, as shown in Fig. 12. It is observed from Fig. 12 that the COF decreases with an increase in the load. This is ascribed to the development of a protective oxide layer (generally developed at a temperature between 150-250 °C). At lower temperatures, there is a reduction of metal to metal contact surface area due to debris of oxide, which results in the reduction of friction and wear rate (Ref 30). The Fe-Ni alloy exhibited the maximum COF of 1.6 at 5 N, while the Fe-42% Ni-2% Y_2O_3 alloy showed the minimum COF of 0.5 at 20 N. The addition of Y_2O_3 in Fe and Fe-42% Ni showed a decrease in the COF as it promotes the formation of oxide rich layer at the contact surface. Further, fluctuations in the COF are observed for the compositions containing complex hard oxide particles developed due to yttria addition, which played an important role in the frictional mechanisms.

Typical surface profiles of the wear tracks obtained after wear testing of the SPSed samples are shown in Fig. 13. The depth of wear track is measured to vary from 5–20 µm as the sliding load changed from 5 to 20 N. Again, the Fe-42% Ni sample exhibited the maximum depth, while the Fe-42% Ni-2% Y_2O_3 alloy exhibited the minimum wear depth. The sample (Fe-42% Ni-2% Y_2O_3) showing the maximum hardness revealed the minimum wear depth, which correlates the properties of the material well.

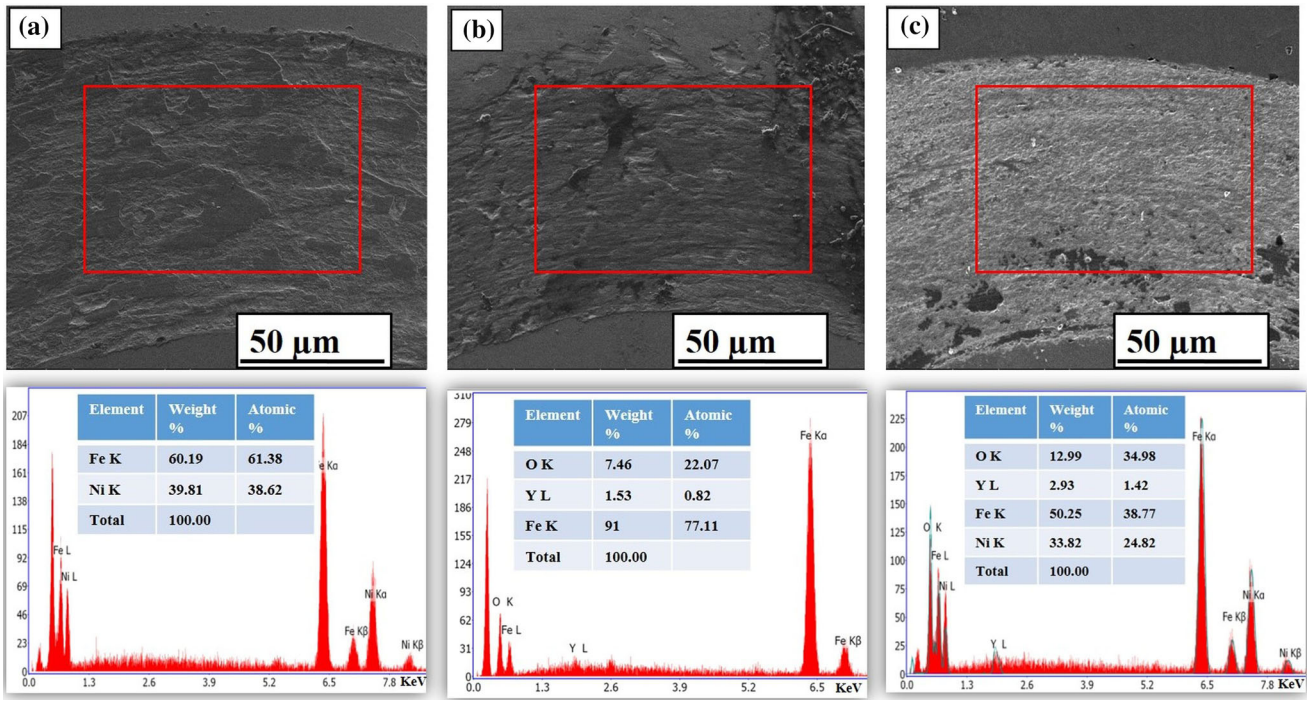

Fig. 14 SEM micrograph of worn surfaces at 20 N load of (a) Fe-42% Ni, (b) Fe-2% Y_2O_3, (c) Fe-42% Ni-2% Y_2O_3 alloys sintered at 1000 °C

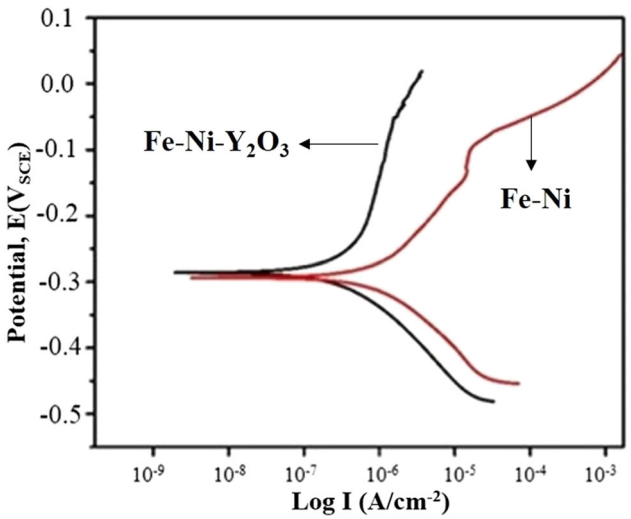

Fig. 15 Potentiodynamic polarization scans for Fe-42% Ni-2% Y_2O_3 and Fe-42% Ni alloys sintered at 1000 °C

Worn surfaces of the SPSed samples recorded by SEM are shown in Fig. 14. All the worn surfaces show the presence of abrasion grooves. However, the Fe-42% Ni-2% Y_2O_3 samples shows a relatively smoother surface with a layered structure. Thus, the dominant wear mechanism is found to change from abrasion to adhesion. As the sliding wear occurred in ambient conditions, the layers formed at high load are believed to be rich in oxides. Referring to XRD analysis (Fig. 5) of the SPSed samples, the presence of Fe_3O_4 and NiO in the case of Fe-42% Ni-2% Y_2O_3 sample is believed to contribute to a large extent of formation of oxide rich layer at the contact surface. The COF and wear depth are also minimum in case of the Fe-42% Ni-2% Y_2O_3 sample.

Table 1 Results obtained from potentiodynamic polarization test for the samples sintered at 1000 °C

Samples	E_{corr}, mV vs. SCE	I_{corr}, µA/cm^2
Fe-42% Ni	− 293.0 mV	1.34
Fe-42% Ni-2% Y_2O_3	− 288.0 mV	0.78

3.7 Corrosion Behavior

The potentiodynamic polarization behavior of the Fe-42% Ni and Fe-42% Ni-2% Y_2O_3 samples sintered at 1000 °C is shown in Fig. 15, and detailed results are presented in Table 1. A comparison of the corrosion rate of the Fe-2% Y_2O_3 sample with that of the Fe-42% Ni and Fe-42% Ni-2% Y_2O_3 is not justified, as in the Fe-2% Y_2O_3 sample, the major amount is Fe (98%), which is not suitable for corrosion resistance. The main comparison is made between Fe-42% Ni and Fe-42% Ni-2% Y_2O_3 systems due to the presence of the same amount of Ni (42%), which plays a significant role in corrosion resistant property in Fe alloys (Ref 3). From the polarization curve, E_{corr} and I_{corr} values are calculated by the Tafel extrapolation method (Ref 31).

It is found that the corrosion resistance of Fe-42% Ni-2% Y_2O_3 was slightly better than that of the Fe-42% Ni alloy. The current density, I_{corr} is found to decrease from 1.34 µA/cm^2 for the Fe-42% Ni to 0.78 µA/cm^2 for the Fe-42% Ni-2% Y_2O_3 sample. Appropriate addition of Y_2O_3 could reduce the oxidation rate and increase adhesion between oxide layers and substrate. This is possibly beneficial to improve exfoliation resistance of the oxide layers. The presence of a stable oxide layer in the Fe-42% Ni-2% Y_2O_3 sample is attributed to the resistance against corrosion (Ref 11).

4. Conclusions

The present study deals with the investigation of the preparation and characterization of 2% Y_2O_3 added Fe-42% Ni alloy in comparison to the Fe-42% Ni and Fe-2% Y_2O_3 samples. At first, as received Y_2O_3 powder sample was milled for 40 h to reduce the particle size to 30-60 nm. The mechanically alloyed samples were sintered by SPS at 800, 900, and 1000 °C. Sintering characteristics, mechanical properties, wear, and corrosion behavior have been correlated with the microstructural features and its subsequent stability. The major findings are:

- The density of sintered samples increased with an increase in sintering temperature. The addition of Y_2O_3 in Fe-42% Ni caused a decrease in the crystallite size after mechanical alloying. With increase in the sintering temperature, the microhardness of the SPSed samples decreased due to grain coarsening in spite of the increase in the sintered density.
- The addition of 2% of nanosize Y_2O_3 increased the hardness about 35% from 5.8 GPa to 7.9 GPa. The Fe-Ni alloy sample without any Y_2O_3 exhibited the maximum wear in dry sliding against alumina ball, while the Fe-42% Ni-2% Y_2O_3 sample exhibited the minimum wear due to the presence of complex, hard and nanoscale oxides.
- The corrosion resistance of Fe-42% Ni-2% Y_2O_3 was slightly better than the Fe-Ni sample SPSed at 1000 °C. Overall, the present research essentially indicates that the effect of the addition of 2% Y_2O_3 is beneficial for the mechanical, wear, and corrosion behavior of Fe-42% Ni alloy.

Acknowledgment

Metallurgical and Materials Engineering Department and Institute Instrumentation Center, IIT Roorkee are highly acknowledged for granting all the facilities required to carry out the research work.

References

1. M.S. Chuang and S.T. Lin, Effects of Phosphorus Addition on the Magnetic Properties of Sintered Fe-50 wt% Ni Alloys, *J. Mater. Eng. Perform.*, 2003, **12**, p 23–28
2. D. Nayak, Grain Size Stabilization of Fe and Fe-Ni Nanostructures Developed by Alloying, Thesis, 2013
3. N. Singh, O. Parkash, and D. Kumar, Phase Evolution, Mechanical and Corrosion Behavior of Fe(100-x) Ni(x) Alloys Synthesized by Powder Metallurgy, *J. Phys. Chem. Solids*, 2018, **114**, p 8–20
4. N. Alharthi, E.M. Sherif, H.S. Abdo, and S.Z. Abedin, Effect of Nickel Content on the Corrosion Resistance of Iron-Nickel Alloys in Concentrated Hydrochloric Acid Pickling Solutions, *ADV MATER SCI, ENG.*, 2017, **6**, p 1–8
5. D. Wenschhof, *Metals Hand Book*, 9th ed., American Society for Metals, Metals Park, OH, 1980, p 792
6. J. Ma, M. Qin, L. Zhang, R. Zhang, and X. Qu, Microstructure and Magnetic Properties of Fe-50% Ni Alloy Fabricated by Powder Injection Molding, *J. Magn. Magn. Mater.*, 2013, **329**, p 24–29
7. H. Kotan, K.A. Darling, M. Saber, C.C. Koch, and R.O. Scattergood, Effect of Zirconium on Grain Growth and Mechanical Properties of a Ball-Milled Nanocrystalline Fe-Ni Alloy, *J. Alloys Compd.*, 2013, **551**, p 629–631
8. P. Susila, D. Sturm, M. Heilmaier, B.S. Murty, and V. Subramanya Sarma, Microstructural Studies on Nanocrystalline Oxide Dispersion Strengthened Austenitic (Fe-18Cr-8Ni-2W-0.25Y_2O_3) Alloy Synthesized by High Energy Ball Milling and Vacuum Hot Pressing, *J. Mater. Sci.*, 2010, **45**, p 4854–4865
9. O.A. Graeve, R. Kanakala, L. Kaufman, K. Sinha, E. Wang, B. Pearson, G. Rojas-George, and J.C. Farmer, Spark Plasma Sintering of Fe-Based Structural Amorphous Metals (SAM) with Y_2O_3 Nanoparticle Additions, *Mater. Lett.*, 2008, **62**, p 2988–2991
10. H. Kotan, K.A. Darling, R.O. Scattergood, and C.C. Koch, Influence of Zr and Nano-Y_2O_3 Additions on Thermal Stability and Improved Hardness in Mechanically Alloyed Fe Base Ferritic Alloys, *J. Alloys Compd.*, 2014, **615**, p 1013–1018
11. D. Sun, C. Liang, J. Shang, J. Yin, Y. Song, W. Li, T. Liang, and X. Zhang, Effect of Y_2O_3 Contents on Oxidation Resistance at 1150 °C and Mechanical Properties at Room Temperature of ODS Ni-20Cr-5Al alloy, *Appl. Surf. Sci.*, 2016, **385**, p 587–596
12. C.C. Koch, Synthesis of Nanostructured Materials by Mechanical Milling: Problems and Opportunities, *Nanostruct. Mater.*, 1997, **9**, p 13–22
13. E.K. Park, S.M. Hong, J.J. Park, M.K. Lee and C.K. Rhee, An Investigation on Stability of Y_2O_3 and Sintering Behavior of Fe-Base ODS Particles Prepared by High Energy Ball Milling, 18th International Conference on Composite Materials, 2011, 20, p 13-22
14. H. Kasturi, T. Paul, S. Biswas, and S.H. Alavi, Sliding Wear Behavior of Spark-Plasma-Sintered Fe-Based Amorphous Alloy Coatings on Cu-Ni Alloy, *J. Mater. Eng. Perform.*, 2018, **27**, p 3629–3635
15. G. Cui, X. Wei, E.A. Olevsky, R.M. German, and J. Chen, Preparation of High Performance bulk Fe-Ni Alloy by Spark Plasma Sintering, *Mater. Des.*, 2016, **90**, p 115–121
16. M. Laurent-Brocq, F. Legendre, M.H. Mathon, A. Mascaro, S. Poissonnet, B. Radiguet, P. Pareige, M. Loyer, and O. Leseigneur, Influence of Ball-Milling and Annealing Conditions on Nanocluster Characteristics in Oxide Dispersion Strengthened Steels, *Acta Mater.*, 2012, **60**, p 7150–7159
17. M. Saber, W. Xu, L. Li, Y. Zhau, C.C. Koch, and R.O. Scattergood, Size Effect of Primary Y_2O_3 Additions on the Characteristics of the Nanostructured Ferrite ODS Alloys: Comparing as-Milled and as Milled/Annealed Alloys Using S/TEM, *J. Nucl. Mater.*, 2014, **452**, p 223–229
18. I. Hilger, M. Tegel, M.J. Gorley, P.S. Grant, T. Weißgärber, and B. Kieback, The Structural Changes of Y_2O_3 in Ferritic ODS Alloys During Milling, *J. Nucl. Mater.*, 2014, **447**(1–3), p 242–247
19. C.L. Fu, M. Krcmar, G.S. Painter, and X.Q. Chen, Vacancy Mechanism of High Oxygen Solubility and Nucleation of Stable Oxygen-Enriched Clusters in Fe, *Phys. Rev. Lett.*, 2007, **99**(22), p 25502
20. Y. Cheng, Y. Qi, P. Hu, S. Zhou, G. Chen, J. An, K. Jin, and W. Han, ZrB_2-SiC-G Composite Prepared by Spark Plasma Sintering of In-Situ Synthesized ZrB_2-SiC-C Composite Powders, *J. Am. Ceram. Soc.*, 2016, **99**, p 2131–2137
21. M.B. Shongwe, S. Diouf, M.O. Durowoju, and P.A. Olubambi, Effect of Sintering Temperature on the Microstructure and Mechanical Properties of Fe-30% Ni Alloys Produced by Spark Plasma Sintering, *J. Alloys Compd.*, 2015, **649**, p 824–832
22. I.M. Makena, M.B. Shongwe, M.M. Ramakokovhu, and M.L. Lethabane, Influence of Temperature on Microstructure and Mechanical Properties of Ni-40 Fe-10 Co Alloy Consolidated by Spark Plasma Sintering, *Procedia Manuf.*, 2017, **7**, p 708–713
23. J. Hidalgo, A.J. Morales, T. Barriere, J. Gelin, and J.M. Torralba, Mechanical and Functional Properties of Invar Alloy for μ-MIM, *Powder Metall.*, 2013, **57**(2), p 127–136
24. M. Ohnuma, J. Suzuki, S. Ohtsuka, S.W. Kim, T. Kaito, M. Inoue, and H. Kitazawa, A New Method for the Quantitative Analysis of the Scale and Composition of Nanosized Oxide in 9Cr-ODS Steel, *Acta Mater.*, 2009, **57**(18), p 5571–5581
25. S. Ohtsuka, S. Ukai, M. Fujiwara, T. Kaito, and T. Narita, Nanostructure Control in ODS Martensitic Steels by Means of Selecting Titanium and Oxygen Contents, *J. Phys. Chem. Solids*, 2005, **66**, p 571–575
26. E. Gil, N. Ordás, C. García-Rosales, and I. Iturriza, ODS Ferritic Steels Produced by an Alternative Route (STARS): Microstructural Characterization After Atomization, HIPping and Heat Treatments, *Powder Metall.*, 2016, **59**, p 359–369
27. R.S. Azis, M. Syazwan, and M.M. Shahrani, Influence of Sintering Temperature on the Structural, Electrical and Microwave Properties of Yttrium Iron Garnet (YIG), *J. Mater. Sci.*, 2018, **29**, p 8390–8401

28. V.M.S. Muthaiah and S. Mula, Influence of Cr and Y Addition on Microstructure, Mechanical Properties, and Corrosion Resistance of SPSed Fe-Based Alloys, *Metall. Mater. Trans. A*, 2018, **49**, p 990–1005
29. S.R. Bakshi and V. Musaramthota, Spark Plasma Sintered Tantalum Carbide-Carbon Nanotube Composite: Effect of Pressure, Carbon Nanotube Length and Dispersion Technique on Microstructure and Mechanical Properties, *Mater. Sci. Eng. A.*, 2011, **528**, p 2538–2547
30. A. Mishra, Reduction of Sliding Wear of Alloys by Using Oxides, *Int. J. Mech. Eng. Robot. Res*, 2014, **3**(3), p 598–602
31. A. Kumar, S. Sharma, K. Pal, and S. Mula, Effect of Process Parameters on Microstructural Evolution, Mechanical Properties and Corrosion Behavior of Friction Stir Processed Al 7075 Alloy, *J. Mater. Eng. Perform.*, 2017, **26**, p 1122–1134